Lawrence Livermore Laboratory

Diagnostics for the Laser Fusion Program - Plasma
Physics on the Scale of Microns and Picoseconds

David T. Attwood

May 19, 1978

MASTER

DIAGNOSTICS FOR THE LASER FUSION PROGRAM - PLASMA PHYSICS ON
THE SCALE OF MICRONS AND PICOSECONDS*

David T. Attwood
University of California
Lawrence Livermore Laboratory
Livermore, CA 94550, USA

Introduction

Laser induced fusion is the forerunner of a class of inertial confinement
schemes in which hydrogen isotopes are heated to thermonuclear conditions in
a very short period. The process is characterized by such short time scales
that fuel confinement is achieved through its' own finite mass and expansion
velocity, approaching 1 µm/psec for ignition temperatures of order 10 keV
(10^8 °K). With current laser powers limited to several terrawatts one readily
estimates, on the basis of energy conservation, target mass, and expansion ve-
locity, that target size and laser pulse duration are on the order of 100 µm
and 100 psec, respectively. Within these constraints, targets have been heat-
ed and confined to the point where thermonuclear conditions have been achieved
This paper describes a sampling of diagnostic techniques with requisite resolu-
tion (microns and picoseconds) to accurately describe the dynamics of a laser
driven compression. As discussed in each case cited, these in turn provide
insight to and quantitative measure of, the physical processes dominating the
implosion. The success of the inertial confinement fusion program is strongly
dependent on the continued development of such diagnostics and the understand-
ing they provide.

Target Considerations - What are we Trying to Diagnose?

In this section we briefly review the implosion dynamics of two representative
classes of inertial confinement targets. The ablatively driven target of Fig.
1, first described by NUCKOLLS et al. [1] in 1972, is that of an idealized
deuterium-tritium (D-T) liquid droplet designed to achieve both high density

hν   hν

D-T liquid

hν

hν

Shaped
nanosecond
laser
pulse

Intensity

Time

Fig. 1 Ablatively driven
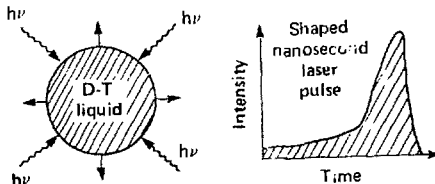laser fusion target.

and high temperature with a several nanosecond duration shaped laser pulse.
It is instructive in this case to represent the long laser pulse as a series
of short pulses of increasing peak intensities. These relatively weak pulses
are absorbed in a rather benign fashion, causing surface heating and ablation
of a small amount of material radially outward from the spherical surface.

Newton's third law states that for every action there is a reaction, producing a rocket like effect whereby the ejected (ablated) material causes the remaining material to accelerate inward, initiating the implosion process. Ever increasing optical intensities then continue to launch similar weak, but increasingly strong shocks towards the target center. The laser pulse profile is designed to have all the spherically converging shocks coalesce at the still unheated target center. By protecting the core from pre-heat, maximum compression can be obtained. With simultaneous compression and heating of a small core region, thermonuclear ignition conditions are achieved, followed by a burn which propagates outward through the remaining fuel. The primary difficulties with this design, partially contemporary, are that it requires a peak laser power of $\sim 10^{15}$ watts, a factor of 100 larger than currently available, it provides no protection from the nonthermal electrons associated with the absorption of intense light, and it provides no unusual leverage against Rayleigh-Taylor type fluid instabilities -- the primary concern in high compression experiments. Nonetheless, it gives insights to the essential dynamics of ablatively driven targets. A review of more sophisticated options is discussed in [2].

A simpler class of experiments, which avoid the stability problem and work well with available lasers (0.5 to 20 TW), are described in Fig. 2. These
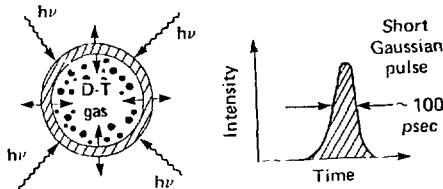

Fig. 2 Thin "exploding pusher" target.

thin shelled targets operate in a significantly different manner than those considered above. Being irradiated by a very short laser pulse, the glass shell heats rapidly to a keV temperature before significant shell expansion can take place. The heated shell then explodes violently, both inward and outward, with the inward directed glass or pusher compressing the encapsulated D-T fuel in the process [3]. In addition to adapting to presently available laser powers and avoiding fluid instability problems, the "exploding pusher" targets offer several other advantages. The design uses rather than avoids electron preheat, and by working with short laser pulses avoids the development of long density gradients in the plasma atmosphere where stimulated parametric processes, such as Brillouin scattering, can reflect away much of the incident light before it is absorbed. In short, exploding pusher targets have permitted the laser fusion program to proceed with the development of diagnostics and complex computer codes during a period in which lasers of sufficient power to drive an ablative implosion were not available.

Of course nothing is free. The cost of producing high temperatures with small energies is that the reacting mass is small and not very dense. The cost of avoiding fluid instabilities is that of reaching densities not much higher than those started with. Rather than compressing a liquid droplet from 0.1g/cc to 1000g/cc and initiating a thermonuclear burn wave, we begin with a DT gas at .001g/cc and drive it to little more than 0.1g/cc. However, as stated above, a firm foundation is now available for the study of intermediate and high density implosions which lie ahead. This will help us in

the near term as we begin the delicate tradeoff of temperature for density, attempting to travel as far as possible along the compression route while maintaining temperature at a sufficiently high level to produce a diagnose-able reaction level. From the vantage point of experience then, we will re-view selected experiments of the "exploding pusher" type, considering them as a prelude to the more difficult problems of symmetry and stability associ-ated with the high density experiments which lie ahead.

To consider the pertinent diagnostics for a given target we isolate those regions where significant processes take place and give an estimate of the relevant physical parameters therein. Figure 3 shows such a diagram for an exploding pusher target. Briefly reviewing the implosion dynamics, energy

Plasma atmosphere
optical absorption,
10^{20}-10^{21} e/cc

Ablation region
energy transport,
10^{21}-10^{23} e/cc

Fully ionized pusher
glass shell, $\sim 10^{24}$ e/cc

Compressed fuel
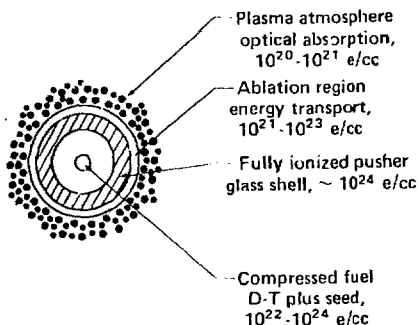D-T plus seed,
10^{22}-10^{24} e/cc

Fig. 3 Diagnostics of a fuel pellet are addressed to regions dominated by differing physical processes and conditions.

from a short intense laser pulse is partially absorbed in the plasma atmos-phere, or corona. The fractions of absorbed energy going to thermal and non-thermal particle distributions is dependent on the absorption mechanism. For a steep gradient plasma, typical of short pulse irradiations, absorption is primarily by resonance absorption, a process in which most of the abosrbed energy appears in suprathermal electrons. These hot electrons have long mean ee paths, enabling them to quickly and uniformly heat the entire glass nell to keV like temperatures. The heated shell then expands explosively, in both directions, viz, with approximatley equal masses going radially in nd radially out. The inner portion of the shell continues to move radially in, driving the encapsulated D-T gas with it until the internal pressure of the gas is sufficient to produce a stagnation condition. At stagnation the mean directed motion of the implosion, which has now been transferred elec-trostatically to the heavier ions, is quickly converted to thermal energy. This drives the fuel ions to thermonuclear temperatures (10-20 keV). The reactions are quenched in several tens of psec, for this type implosion, by collisions with the colder electrons. A somewhat surprising aspect of this description is the relatively minor role played by thermal electron conduc-tion of energy from the corona to the pusher. Transport of energy by this mechanism appears from simulations [3] to be inhibited by a factor of about 30 from classical values. Two candidate mechanisms for this inhibition are the presence of randomly oriented megagauss microscopic magnetic fields, and very strong collective density fluctuations, each of which would deflect thermal electrons from given trajectories and thus reduce the flow of energy from the hot plasma corona to the cooler glass shell. Each aspect of the

energy transfer process just outlined, from laser to fuel, must now be studied experimentally to cunfirm both qualitatively and quantitatively that the dynamics are correct as stated.

Probing the Plasma Atmosphere

The plasma atmosphere is the relatively low density region surrounding the pellet where laser light is absorbed. It is formed by ablation of material from the target surface. In short pulse laser experiments, typically 100 psec duration the radial gradient of electron density is very sharp, e-folding on a scale of sub-micron to 10 microns (μm) or so. The density gradient in this region plays a very important role in the mechanism of light absorption, and through that plays an indirect role in the partition of absorbed energy between thermal and non-thermal particle distributions [4]. As outlined in Fig. 4, there are three basic mechanisms through which intense laser
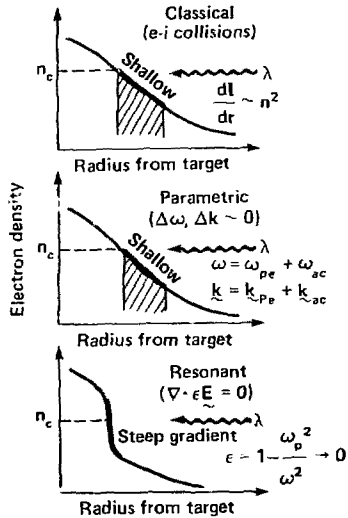
Fig. 4 Absorption of intense laser light is by three competing mechanisms.

light may interact with the plasma as it approaches the reflection or turning point in density where a given wavelength of light can no longer propagate. That density is referred to in plasma physics as the "critical density, n_c". The first mechanism is simple electron-ion collisions, sometimes called "inverse bremsstrahlung", where the electric field of the incident light rattles electrons, who then lose this energy in classical collisions with ions. The mechanism depends on both electron and ion density, thus increasing as n^2 as the wave approaches the critical density (or reflection point). This mechanism is obviously more important with slowly varying density gradients, as indicated in Fig. 4A, since the interaction volume for high n^2 is larger. The parametric processes of Fig. 4B also work most efficiently when the gradient is shallow. These are stimulated processes in which an intense (above threshold) laser field drives one or more acoustic waves out of the noise in a three wave parametric interaction. The dispersion properties of the acoustic waves are density dependent so that appreciable growth occurs only over

fairly shallow density profiles. Both absorptive and reflective instabilities are possible depending on whether both or only one of the stimulated waves is acoustic. A typical absorptive process is the ion-acoustic or "parametric decay" instability in which laser light decays into a high frequency electron acoustic wave and a low frequency ion-acoustic wave, conserving energy and momentum as indicated in Fig. 4B. An important reflective instability is stimulated Brillouin scattering in which the incident laser light decays into an ion wave and a slightly downshifted electromagnetic wave. As before, these processes are generally expected to play significant roles in shallow gradient plasmas formed by intense laser light in the nanosecond regime. For shorter pulse experiments the expanding plasma does not extend very far, tens of microns, before the pulse is over. An important short pulse, short gradient absorption mechanism is the rather poorly termed "resonance absorption" of Fig. 4C. In this case the gradient is sufficiently short that the field strength of the wave reaching critical density is quite large. For p-polarized light obliquely incident on the plasma surface, a radial component of electric field exists at the "plasma resonance" where the dielectric constant of the medium goes to zero, viz, $\epsilon_p = 1 - \frac{n}{n_c} = 0$. With the boundary condition $\nabla \cdot \epsilon_p E = 0$ at the critical surface there is indeed a resonance, and depending on gradients and loss mechanisms, the field amplitudes may be very large causing a large transfer of energy to electrons in this region. The mechanism is of course angle and polarization dependent, and will only play a significant role where refractive turning of the incident light permits a strong field component to tunnel to the critical surface

In summary three different mechanisms are available for the absorption of light, contributions of each depending on the density gradient and temperature of the plasma, and on the intensity, polarization and angle of incidence of the laser light. With only inverse bremsstrahlung (collisional absorption) leading to a thermal distribution of particle energies, the dominance of one mechanism over the others has a profound impact on implosion dynamics. We will see in the following that for short pulse experiments, finite expansion times, radiation pressure effects, and localized heating can combine to produce short scale lengths assuring the dominance of resonance absorption and the concomitant production of suprathermal electrons alluded to previously in the description of implosion dynamics.

To estimate expected scale lengths we consider typical plasma expansion velocities and pulse durations. For an SiO_2 plasma ablating from a pellet surface at 1 keV, the average ion mass is about 20 m_p so that on the basis of charge neutrality one expects an expansion velocity of order 0.1 μm/psec. For a pulse duration of 100 psec, typical of exploding pusher experiments, one estimates scale lengths to be of order 10 μm. Other factors conspire to reduce this value. For instance, radiation pressure due to the incident light itself may cause density profile steepening or critical surface deformation on both a small and large scale. Representative cases and nomenclature are described in Fig. 5. Both of these features have been observed in recent experiments[5].The most successful technique used to date for studying the plasma atmosphere is that of optical probing in the classical sense of interferometry, polarimetry, etc., except that the densities and gradients demand a wavelength in the ultraviolet. Figure 6 shows the general technique in which a probe pulse of wavelength λp passes transversely through the plasma, its phase and polarization being modified by the refractive index of this ionized medium. The pulse must be temporally short to avoid smearing as the plasma density contours move outward, typically with velocities of order 0.1 μm/psec. For an interferometer with fringe spacings of about 1 μm one then

requires a probe duration of $\sim$ 10 psec. Refractive turning of the probe through an angle θ, as in Fig. 6, must be minimized so that the ray is not lost to the collecting optics. For axial scale lengths of 1 μm and transverse dimensions of 20 μm, one requires a probe wavelength in the ultraviolet in order to probe critical densities.
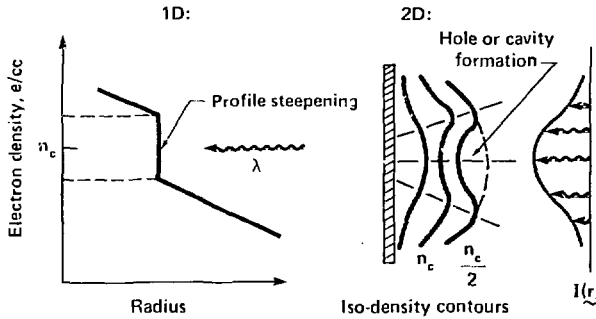

Fig. 5 Two manifestations of radiation pressure are described. Finite momentum transfer by a large photon flux push and distort the expanding plasma.

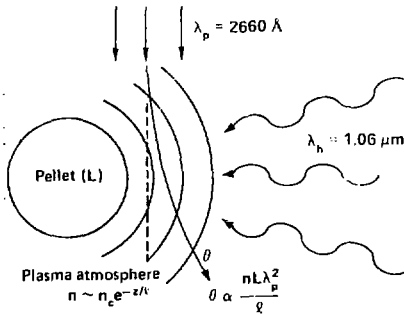

Fig. 6 The effect of refraction on optical probing is seen to depend on wavelength squared, and inversely on the axial scale length.
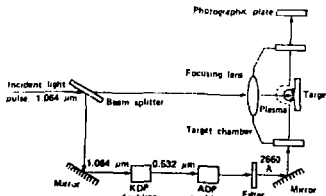

Fig. 7 Scheme for producing synchronous UV diagnostic pulse with stacked frequency doubling crystals.

The technique for obtaining a synchronous optical probe is shown in Fig. 7.
Just after the oscillator switchout a portion of the main laser pulse is
reflected into a separate beam filtering, shaping and amplifying chain.
Non-linear phase distortion is maintained below tenth wave. Amplification
is followed by cascaded frequency doubling, for an overall wavelength change
from 1.064 μm to 2660 Å. Conversion efficiency in each case is maintained
at no more than 10% so as to maximize pulse shortening effects. The 30 psec
infrared pulse then exits as an apprxoximately 15 psec ultraviolet pulse.
The UV pulse is then directed towards the target chamber for diagnostic use.
The interferometer used is shown in Fig. 8. Its holographic nature is par-
ticularly useful in obtaining near diffraction limited resolution ($\lesssim$ 1μm),
and providing accurate focusing in the central target plane. Focusing accu-
racy of several microns is desireable but difficult to obtain with a pulsed
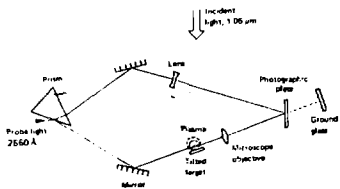UV source and inherent mechanical drift. By imaging after the fact with CW

Fig. 8 Holographic system used for
diffraction limited, accurately focus-
able interferometry. A key element is
the 0.2 NA ultraviolet transmitting
microscope objective.
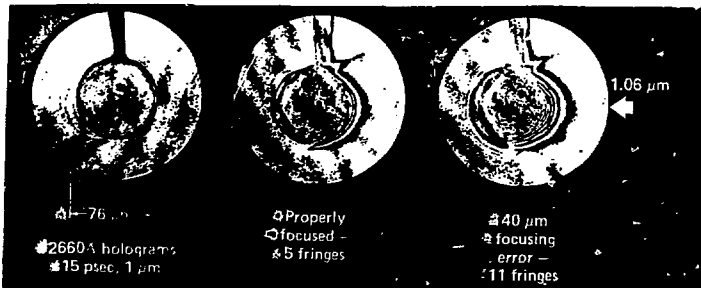
Fig. 9 Fringe pattern is a strong function of image plane position in a
steep gradient plasma. This can lead to serious errors of misinterpretation
if a variable focus holographic system is not used.

He-Ne reconstruction procedures, these difficulties vanish. An example of
focusing effects is shown in Fig. 9, where the effect of a 40 μm focusing
"error" produces a different fringe pattern. This is not a difficulty here,
but would be in a classical interferometer.

An example of a well focused interΩgram, along with its analysis, is shown
in Fig. 10. In this target experiment a 41 μm diameter glass microballon was

Fig. 10 Profile steepening due to radiation pressure is demonstrated in this target irradiation experiment $I \approx 3 \times 10^{14}$ W/cm^2.

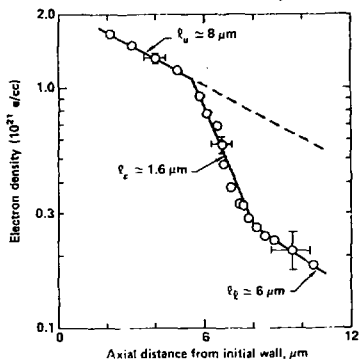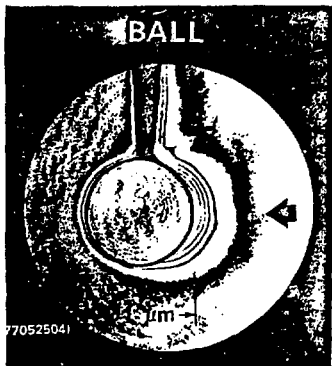irradiated with a 30 psec, 1.06 μm laser pulse at an intensity of 3×10^{14} W/cm^2. The resulting interferogram has been Abel inverted, with axial electron densities plotted to the right. These results demonstrate that <u>radial</u> density profiles are indeed steepened by radiation pressure effects. A simple but instructive model for this effect is to consider a static balance of partial pressures at the critical surface, where the high density side has only particle pressure, while the lower density laser side has both a thermal (particle) component and a portion due to momentum transferred by photon reflections, viz., $n_u \kappa T = n_l \kappa T + 2I_o/c$, where n_u and n_l are the upper and lower shelf density, κT is the thermal temperature, I_o is the laser intensity and c is the speed of light. The model must then be modified for flow field dynamics, temperature differences across the interface, and finite absorption on a finite density profile. Typical numbers indicate an equivalence of thermal and radiation pressures at 10^{21} e/cc, 1 keV temperature, and a laser intensity of 3×10^{15} W/cm^2. The density step in Fig. 10 is thus somewhat larger than expected, probably due to temperature differences localized by inhibited energy transport in the critical region.

As a practical matter, these results show that for 30 psec experiments the scale lengths are everywhere less than 10 μm, and approximately 1 μm near the critical surface. Referring to fig. 4, this measured profile suggests that resonance absorption plays the major role in absorbing laser light. The shallow profile of 100 μm scale length or larger, required for efficient absorption by classical inverse bremsstrahlung or parametric decay, does not exist. Further confirmation of density contour deformation is observed in our experiments with flat disk targets, often referred to as "lollypops". An example is shown in Fig. 11, with the Abel inverted densities shown to the right for a plane <u>transverse</u> to the incident light. This is an example of the second case of <u>radiation</u> pressure described previously in Fig. 5B, that due to the transverse profile of the incident light. The cavity or hole formation shown in Fig. 11b has a transverse scale approximately equal to the incident light. Although the data here was numerically inverted,
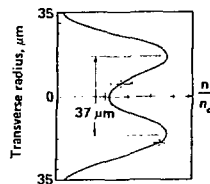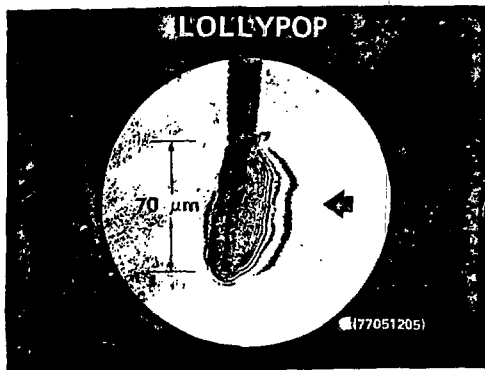
Fig. 11 Cavity formation due to radiation pressure is demonstrated in these flat disk experiments. $I \approx 3 \times 10^{14} W/cm^2$.

$F^\pi \propto \int n ds \sim nL$

$\delta F^\pi \sim \delta(nL) \sim L\delta n$

Flat density contours ➤ Bowed fringes

— — — —Conversely— — — —

Density hole or cavity ◀ Flat fringes

Fig. 12 Simple arguments show that flat fringes in an axisymmetric experiment indicate a density void.

Fig. 13 Locally rippled fringes suggest density fluctuations of 20% amplitude and 10 µm scale size. $I \approx 3 \times 10^{15} W/cm^2$.

inversion is not required to appreciate the presence of a density void. The mere appearance of flat fringes is sufficient to draw this conclusion. Figure 12 sketches this reasoning by pointing out that ray paths are longer through the center of an axisymmetric plasma and therefore should provide larger phase shifts, which would give the appearance of outwardly bowed fringes. By a reversed reasoning, flat fringes imply a density void. In addition to large scale density cavities, we have also observed small scale rippling of the critical surface in our higher intensity experiments with parylene lollypop targets. An example is shown in Fig. 13. As argued in the lower left of Fig. 12, localized fringe variations are primar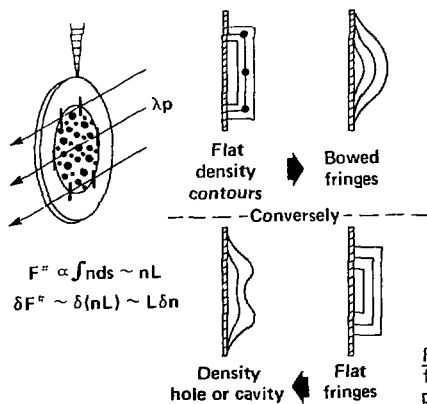ily due to density changes since optical path lengths are essentially equal within small areas of the target. These density variations are most likely produced by hot spots in the incident light beam which push electrons out of their way through the increased radiation pressure. This process is unstable since the low density region is of higher refractive index, thus tending to focus the incident light further. This process of "filamentation" causes a localized mixing of angle and polarization of the incident wave, leading to a smoothing of measured absorption characteristics expected for the dominant resonance absorption process. In addition, these localized ripples very likely have strong surface currents due to the partial absorption of light (transverse momentum of the partially reflected waves is not conserved, a portion having been transferred to the electrons). These randomly oriented surface currents would then lead to randomly oriented magnetic fields, estimated by particle-in-cell computer simulations to be in the megagauss range [6]. These random microscopic fields are not to be confused with the somewhat larger scale toroidal fields due to full target size $\nabla n \times \nabla T$ gradients, which have not yet been observed in laser fusion targets [7]. The great interest in strong microscopic fields is, of course, directed at understanding the reduction of energy transfer via electron conduction, which is observed indirectly in implosion experiments, an example of which will be presented in the next section. Although simulations also suggest strong ion density fluctuations, which would also reduce electron conduction by strong scattering, measurements which demonstrate such effects have not yet been devised.

Dynamics of the Pusher

The previous section discussed the mechanisms for light absorption, comments regarding hot electron production, and possible cause for the inhibition of energy transport by thermal electrons. In this section we discuss measurements of pusher dynamics which provide a basis for quantitatively testing the resultant exploding pusher model. These observations are made possible by strong x-ray self-emission from the hot ($\sim$ 1 keV), dense ($\sim 10^{24}$e/cc)
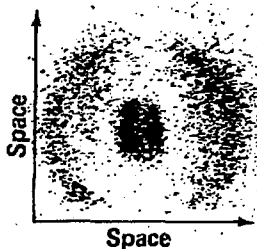

Fig. 14 Time integrated (<200 psec) x-ray image of a laser imploded target. Total laser power was 0.5 TW, focused with a pair of 0.99 NA clamshells to this 126 μm diameter microballoon.

shell, as described in reference to Fig. 3. An example of such emission is given by the time integrated x-ray image of Fig. 14, obtained in this case with an x-ray microscope [8]. The outer ring of x-ray emission occurred during the early phase of laser heating, before the shell exploded. Brightest emission regions are associated with spatially intense areas of the incident light. Upon explosion, density drops everywhere reducing the intensity of x-ray emission below detection threshold. Density, and hence x-ray emission rise again at the target center as the inner half of the shell stagnates against the compressed fuel. Measurement of the "implosion time" between these x-ray emission peaks can provide an estimate of the average implosion velocity $\bar{v} = \Delta r/\Delta t$. Typical values are 2-4 x 10^7 cm/sec [9]. Figure 15 shows a simplified schematic of an x-ray streak camera whose temporal resolution is 15 psec. The time modulated x-ray envelope strikes a slit shaped
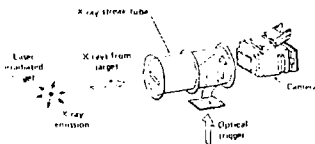

Fig. 15 Schematic of x-ray streak camera for detection of 1-20 keV x-rays with 15 psec resolution.

gold photocathode emitting a similar envelope of secondary electrons. The slit image is then focused by electron optics at a visible phosphor screen. Deflection electrodes sweep the slit shaped electron beam across the surface, displaying the temporal modulation thereon, i.e., the temporal x-ray bursts are spatially separated in the vertical direction of Fig. 15. Sample x-ray signatures are shown in Fig. 16 for three experiments with 82 μm diameter,
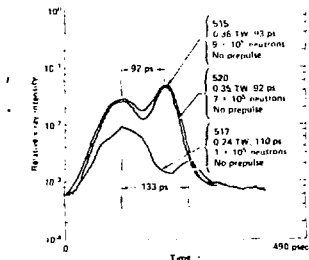
Fig. 16 Time resolved x-ray emission from three laser compressed targets. Differing signatures show the effects of laser power and pulse duration on implosion time. Use of a chlorine filter limits x-rays in this channel to 2.3 - 2.6 keV. Several channels are simultaneously detected.

diameter, 1.7 μm thick glass shell targets [10]. Although it is encouraging to obtain mean velocities in this manner, the technique leaves a great deal to be desired. First of all, it provides only a mean velocity, not the detailed implosion history required to elucidate the important physical processes. Further, the technique is susceptible to interpretive errors when the x-ray bursts are not well separated, as occurs for example with smaller target radii and wall thickness than used for Fig. 16.

A better method for measuring implosion velocities is to combine imaging and temporal recording in a single measurement, as illustrated in Fig. 17. A 6 μm diameter pinhole [11] is used to form an image of the target, in

Fig. 17 Time resolved x-ray pinhole photography of imploding laser fusion targets.

its own x-ray emission, at the streak camera. Because the photocathode is slit shaped (one-dimensional), only a narrow section of the x-ray image is actually detected. The formation of a space-time implosion diagram is illustrated in Fig. 18 where an equivalent cathode slit is placed across the
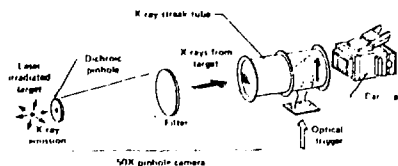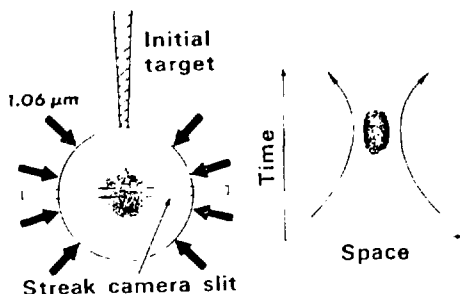

Fig. 18 Construction of a space-time implosion diagram.

target image. Early x-ray emission due to laser heating is from the outermost target regions, followed by peak x-ray emission from the stagnated core. As seen from the streak camera slit, an x-ray emission front appears to propagate inward from both sides. Sweeping action within the streak camera stretches the motion in time, as shown to the right side of Fig. 18. Sample space-time (r,t) implosion diagrams [12] are shown in Figs. 19 and 20 for two-sided and one-sided clamshell irradiations, respectively. Shown are film isodensity contours, monotonically increasing towards the target center. Figure 20 shows no emission from the unirradiated left side at early time, as expected. The dashed lines of Figs. 19 and 20 follow peak x-ray emission as a function of time. That these lines are curved indicates that the pusher is accelerating as the implosion progresses. Fitting a constant acceleration to these trajectories we obtain mean values of 4.2 and 3.4 x 10^{17} cm/sec^2 on the left and right sides, respectively, of Fig. 19. The relation between x-ray emission front propagation and shell-fuel interface motion is addressed in Fig. 21 where calculated results using the computer code LASNEX are compared with the measured results of Fig. 20 after correction for film recording characteristics. The general characteristics are observed to be quite similar. The calculations are extremely valuable in that they include two-dimensional laser irradiation and heating effects, making it possible to separate

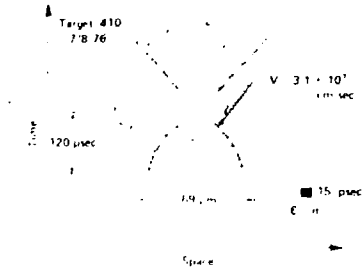Fig. 19 Space-time isodensity contours for a two-sided target irradiation. Density contour interval is 0.2, monotonically increasing towards the target core.
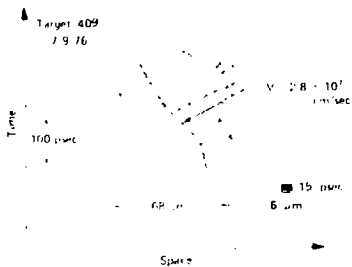
Fig. 20 Same as Fig. 19 for a single-sided target irradiation. Note that target disassembly is two-sided, albeit asymmetric.

and compare propagation of the x-ray emission front (solid line) with the fuel-pusher interface trajectory (dashed line). The inset to the left indicates that less than half the laser pulse played an effective role in this implosion, that is to say, the pulse duration was mismatched to the target radius.

A general feature of these comparisons is that good agreement is obtained for final implosion velocities only when significant inhibition of energy transport by thermal electrons is included. Figure 22 shows calculated velocity and radius histories for three models chosen to test the effects of hot electrons and transport inhibition. Comparison is with the two-sided implosion experiment described in Fig. 19. Best results are obtained [13] (unlabled curves, Fig. 22) when electron conductivities are reduced a factor of 30 below classical values. Without hot electrons pusher acceleration is decreased, but continues for a longer time because of the lower fuel pressure, resulting in similar final velocities but a noticeably different final radius.

Diagnostics of the Heated Core

As considered to this point, laser energy is first absorbed and transported by electrons, eventually equilibriating with ions of the glass pusher. The pusher then explodes, as described in the previous section, transferring a considerable fraction of its random thermal motion to the mean directed motion of the pusher. Because the ions and electrons are constrained electrostatically to move together, the bulk of this mean energy is carried by the
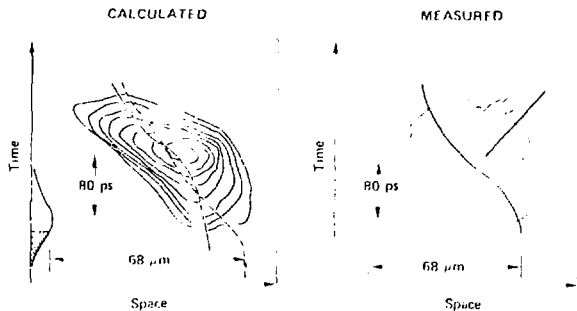
Fig. 21 Calculated and measured x-ray iso-intensity contours for the sin-
gle-sided irradiation experiment of Fig. 20. The calculated solid line rep-
resents peak x-ray emission, while the dashed line traces the fuel-pusher in-
terface J. LARSEN [13].
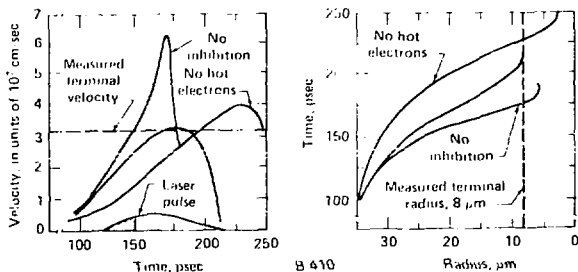
Fig. 22 Numerical simulations of the two-sided implosion of Fig. 19 for
models chosen to test the effects of hot electrons and transport inhibition
on observed implosion dynamics J. LARSEN [13].

heavier ions. Motion of the glass shell drives the encapsulated fuel as
well, also with the bulk of energy residing in the ions. Stagnation is
reached when the pressure of the heated and compressed fuel matches the
dynamic pressure of the pusher. At that point mean motion of the fuel ions
is quickly reconverted to thermal motion, pushing the fuel temperature to
values in the 10 keV range, values sufficiently high for the onset of
thermonuclear reactions among the interacting deuterium (D) and tritium (T)
ions. Calculations indicate that the DT reactions are turned off in about
30 psec by collisional cooling with the relatively cold electrons. Our
study of energy flow from laser to electrons and eventually to thermally
energetic fuel ions is thus complete. The significant point, as far as
diagnostic resolution is concerned is that reaction physics are self-limited
to the psec range, and that one can therefore concentrate efforts on the

development of techniques resolved spatially to microns. Two techniques which have recently provided significant data concerning the compressed core are alpha particle imaging of the burn region through zone plate coded imaging (ZPCI), and density measurements via the observation of x-ray line widths from high-Z seed atoms in the fuel region.

Fig. 23 Zone plate coded imaging (ZPCI) is demonstrated for incoherent emission from three source points. From CEGLIO, [14].

The general technique of ZPCI is shown in Fig. 23. Three incoherent source points cast shadow images of the zone plate coded aperature. The source point emission can be in the form of x-rays, electrons, ions, etc. Geometry is chosen so that diffractive effects play no role in the encoding process. The resultant shadowgraphs, recorded in an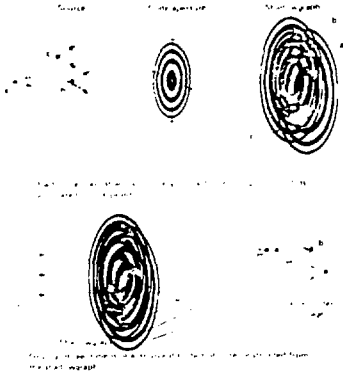 appropriate emulsion or polymer, are then reconstructed with coherent visible light, in this case using the diffractive properties of the zone plate to focus light at three appropriate conjugate points, as shown in the lower portion of Fig. 23. Points B and C, lying in the same plane, produce similar sized, but displaced zone plate shadows, and therefore reconstruct in the same plane. Image brightness is proportional to source brightness. Point A projects a smaller shadow because of its greater distance. Upon reconstruction the smaller zone plate shadow projects a closer image point for A, thus reproducing the three-dimensional nature of the original incoherent source. With free standing gold zone plates of large solid angle, 2.5 μm outer zone width (approximately equal to the resolution) and 10 μm thickness, CEGLIO [14] has exploited this powerful technique with applications to electrons, x-rays, and α-particles. An example is shown in Fig. 24 of the third order reconstructed image of α-particle emission from a laser compressed fusion target. These results prove beyond doubt that detected D-T reactions occur within a small core region of the target and, relying on concurrent α-particle spectroscopy, [15] that the reaction is thermonuclear in nature.

A technique for measuring density (ρ) and density radius (ρr) products in imploded target cores is that of spatially resolving Stark broadened x-ray line emission from high-Z seed atoms. Recent results obtained by YAAKOBI et al., at the University of Rochester are shown in Fig. 25. In addition to the glass lines, they identify the Lyman-α, β, and γ lines of hydrogen like neon. Relative amplitudes indicate that the Ly-α line is optically thick, yielding data concerning ρr, while the optically thin neon Ly-γ line at 1.28

Fig. 24 Third order reconstructed image of the α-particle emitting thermonuclear burn region. Resolution is ~ 3 μm. From CEGLIO, [14].

22 μm

ENERGY (keV)

Fig. 25 Neon and glass x-ray lines from imploded neon-filled microballoon. B. YAAKOBI et al. [16].

keV gives data on the density. Analysis of the latter is shown in Fig. 26. Best fit of the stark profile is for an electron density of 7×10^{22}e/cc at Te = Ti = 300 eV, giving $\rho = 0.26$ g/cc. Analysis of the optically thick Lyman-α line at 1.02 keV gives a ρr value of 2.2×20^{-4}g/cm^2. According to GRIEM, results like this can be pushed to 10^{24}e/cc with less theoretical difficulties by going to x-ray lines of helium-like argon and somewhat larger laser power. Use of these 3 keV lines would then extend the technique to densities of about 5 g/cc, or thirty times the density of liquid DT.

Future Developments

As outlined in the introduction, the current trend of experiments is towards longer pulse, ablatively driven targets with an emphasis on achieving moderate to high densities. The plasma absorption and reflection processes will now have to be restudied in this more shallow gradient environment. Best hopes for ultraviolet probing include use of synchronously driven long and short pulse oscillators [18], combined with pulse shortening regenerative amplifiers 19 and line shifting Raman techniques [7] to get away from harmonic emission from the plasma itself. Sufficiently intense single pulses in the XUV would certainly help beat refraction problems on larger targets.

Ablatively driven implosions are by nature colder than exploding pushers and therefore will not emit copious amounts of x-rays for diagnostics during
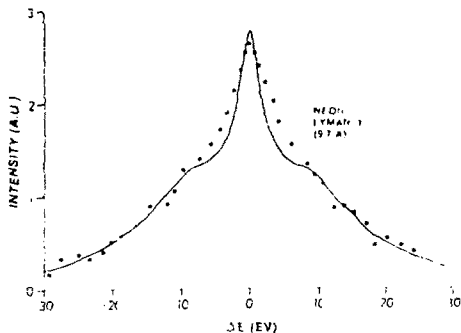
Fig. 26 Stark profile fitting to the neon Lyman-γ line. Best fit is for electron density of 7×10^{22} e/cc at Te=Ti=300 eV. B. YAABKOBI et al [16].

most of the process. For this reason efforts will be required to backlight the implosion with secondary x-ray sources. Preliminary efforts in this direction are already underway at the Rutherford Laboratory in Oxford under the direction of M. Key [20]. At the higher density, higher ρr cores keV x-rays and α-particles will no longer escape, causing us to go to somewhat higher energy x-rays, as well as to thermonuclear reaction products with sufficient range to escape, as suggested by CEGLIO. New techniques must be developed for studying the development of fluid instabilities -- does anyone have a good idea?

Acknowledgments

The author would like to acknowledge informative conversations with W. Kruer, J. Larsen, C. Max, and N. Ceglio. Important measurements not documented here but which are very important for quantitatively successful experiments, are those of target characterization, laser irradiation characteristics (space-time-intensity), and target implosion diagnostics of a space-time integrated nature. Such data is routinely and accurately provided within the LLL laser fusion program by groups under the direction of H. Ahlstrom, L. Coleman, C. Hendricks, and J. Holzrichter.

References

1. J. Nuckolls, L. Wood, A. Thiessen and G. Zimmerman, Nature 239, 179 (1972)
2. J. Nuckolls et al., Laser Program Annual Report-1976, pp 4-1 to 4-121. Lawrence Livermore Laboratory report UCRL-50021-76 (June 1977).
3. J. T. Larsen, "The Dynamics of exploding Pusher Targets for Laser Driven Fusion" (June 1978, unpublished).
4. F. W. Perkins and J. Flick, Phys. Fluids 14, 2012 (1971); C. S. Liu, M. N. Rosenbluth, and R. B. White, Phys. Fluids 17, 1211 (1974); J. P. Freidberg, R. W. Mitchell, R. L. Morse, and L. I. Rudsinski, Phys. Rev. Lett. 28, 795 (1972); K. G. Estabrook, E. J. Valeo and W. L. Kruer, Phys. Fluids 18, 1151 (1975); J. Dawson, P. Kaw and B. Green, Phys. Fluids 12, 875 (1969).
5. D. T. Attwood, D. W. Sweeney, J. M. Auerbach, and P. H. Y. Lee, Phys. Rev. Lett. 40, 184 (1978).

6. K. Estabrook, Phys. Fluids $\underline{19}$, 1733 (1976).
7. J. A. Stamper, E. A. McLean, and B. H. Ripin, Phys. Rev. Lett. $\underline{40}$, 1177 (1978) and reference 10 therein.
8. F. Seward, J. Dent, M. Boyle, L. Koppel, T. Harper, P. Stoering, and A. Toor, Rev. Sci. Inst. 47, 464 (1976); P. M. Campbell, G. Charatis, and G. R. Montry, Phys. Rev. Lett. 34, 74 (1975).
9. C. F. McConaghy and L. W. Coleman, Appl. Phys. Lett. 25, 258 (1974); more accurate comments regarding temporal resolution are given by B. L. Henke, J. A. Smith, and D. T. Attwood, Appl. Phys. Lett. 29, 539 (1977).
10. D. T. Attwood, L. W. Coleman, J. T. Larsen, and E. K. Storm, Phys. Rev. Lett 37, 499 (1976); also, "The Correlation of X-Ray Temporal Signatures, Neutron Yields, and Laser Performance", D. T. Attwood et al., 10th European Conference on Laser Interaction with Matter, Palaiseau, France (1976), UCRL-78739 (unpublished).
11. D. T. Attwood, B. W. Weinstein, and R. F. Wuerker, Applied Optics 16, 1253 (1977).
12. D. T. Attwood, L. W. Coleman, M. J. Boyle, J. T. Larsen, D. W. Phillion, and K. R. Manes, Phys. Rev. Lett. 38, 282 (1977).
13. J. T. Larsen and D. T. Attwood, in preparation.
14. N. M. Ceglio and H. I. Smith, Rev. Sci. Inst. 49, 15 (1978); N. M. Ceglio, J. Appl. Phys. 48, 1563 (1977); N. M. Ceglio, D. T. Attwood, and E. V. George, J. Appl. Phys. 48, 1566 (1977); N. M. Ceglio and L. W. Coleman, Phys. Rev. Lett. 39, 20 (1977).
15. V. W. Slivinsky, H. G. Ahlstrom, K. G. Tirsell, J. Larsen, S. Glaros, G. Zimmerman, and H. Shay, Phys. Rev. Lett. 35, 1083 (1975).
16. B. Yaakobi, D. Steel, E. Thorsos, A. Hauer and B. Perry, Phys. Rev. Lett. 39, 1526 (1977); B. Yaakobi et al., "Explosive Pusher Type Laser Compression Experiments with Neon-Filled Microballons", University of Rochester report URLLE-74 (May 1978, unpublished).
17. H. Griem, Private communication.
18. D. Kuizenga, "Development of An Actively Mode locked and Q-Switched Oscillator for the Laser Fusion Program at LLL", Optical Society of America, Topical Meeting on Picosecond Phenomena (Hilton Head, So. Carolina, 1978), unpublished.
19. J. E. Murray and W. H. Lowdermilk, "The Regenerative Amplifier: A Source for Synchronized, Variable Duration Pulses", ibid.
20. M. Key et al., Topical Meeting on Inertial Confinement Fusion (San Diego, Feb. 1978), unpublished.